JOURNAL OF
SYNCHROTRON
RADIATION

ISSN 1600-5775

High-accuracy X-ray absorption spectra from m*M* solutions of nickel (II) complexes with multiple solutions using transmission XAS

Christopher T. Chantler,[a]* **M. Tauhidul Islam,**[a,b] **Stephen P. Best,**[b] **Lachlan J. Tantau,**[a] **Chanh Q. Tran,**[c] **Mun Hon Cheah**[d] **and Andrew T. Payne**[a]

[a]School of Physics, University of Melbourne, Australia, [b]School of Chemistry, University of Melbourne, Australia, [c]School of Physics, La Trobe University, Australia, and [d]ANU College of Medicine, Biology and Environment, Australian National University, Australia. *Correspondence e-mail: chantler@unimelb.edu.au

Received 17 February 2015
Accepted 26 March 2015

Edited by R. W. Strange, University of Liverpool, UK

Keywords: XAS with uncertainty; hybrid technique; transmission XAS; nickel(II) complexes.

Supporting information: this article has supporting information at journals.iucr.org/s

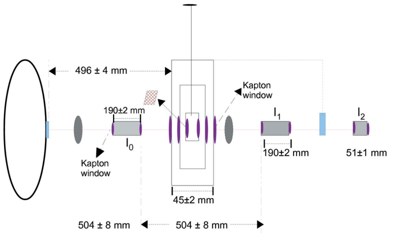

A new approach is introduced for determining X-ray absorption spectroscopy (XAS) spectra on absolute and relative scales using multiple solutions with different concentrations by the characterization and correction of experimental systematics. This hybrid technique is a development of standard X-ray absorption fine structure (XAFS) along the lines of the high-accuracy X-ray extended range technique (XERT) but with applicability to solutions, dilute systems and cold cell environments. This methodology has been applied to determining absolute XAS of bis(*N*-n-propyl-salicylaldiminato) nickel(II) and bis(*N*-i-propyl-salicylaldiminato) nickel(II) complexes with square planar and tetrahedral structures in 15 m*M* and 1.5 m*M* dilute solutions. It is demonstrated that transmission XAS from dilute systems can provide excellent X-ray absorption near-edge structure (XANES) and XAFS spectra, and that transmission measurements can provide accurate measurement of subtle differences including coordination geometries. For the first time, (transmission) XAS of the isomers have been determined from low-concentration solutions on an absolute scale with a 1–5% accuracy, and with relative precision of 0.1% to 0.2% in the active XANES and XAFS regions after inclusion of systematic corrections.

1. Accuracy

Accurate experimental measurements are the key to reliable structural information and the development of theories for X-ray absorption spectra (XAS) analysis. The lack of reliable information on X-ray attenuation and absorption coefficients revealed by several studies (Grodstein, 1957; Cooper, 1965) led to various experimental efforts towards accurate absorption measurements and theoretical tabulations of X-ray mass attenuation coefficients (Hubbell, 1969; Bearden, 1966; Kopfmann & Huber, 1968; McMaster *et al.*, 1969; Kessler Jr *et al.*, 1982; de Meulenaer & Tompa, 1965; Deslattes, 1969). The availability of advanced X-ray sources and development of improved theories have enhanced the development of experimental methodologies (Diaz-Moreno, 2012; Prešeren *et al.*, 2001; Kurisaki *et al.*, 2008; Chantler, 2009) particularly for structural analyses of materials using different sample types. Several particularly insightful and accurate X-ray absorption studies have been verified by developments in theory and by comparison of experimental results (Deslattes, 1959; Hughes *et al.*, 1968; Gerward *et al.*, 1979; Rao *et al.*, 1981; Nathuram *et al.*, 1988), claiming accuracy of around 1%, usually for ideal systems such as elemental metals or monoatomic solids. Further investigation by the International Union of Crystallography led to several archetypal studies of consistency and accuracy in the field (Mica *et al.*, 1985; Creagh & Hubbell, 1987, 1990). This was succeeded by the development of the X-ray extended range technique (XERT) (Chantler *et al.*, 1999; Chantler, 2009, 2010) and the high-accuracy gas-phase techniques of Kodre *et al.* (2006).

XERT has produced the most accurate measurements of X-ray mass attenuation coefficients (Glover *et al.*, 2010; Rae *et al.*, 2010; Islam *et al.*, 2010) using synchrotron radiation, and led to the development of nano-roughness determination (Glover *et al.*, 2009). However, the early methodology was directed towards accurate measurement of mass attenuation, absorption and the atomic form factor for ideal, concentrated, elemental solid samples. Later, the methodology was extended to detailed X-ray absorption fine structure (XAFS) and the accurate determination of these across large energy ranges, but still for ideal concentrated samples (de Jonge *et al.*, 2005; Islam *et al.*, 2014). This in turn stimulated the development of theory, especially including the development of FDMNES (finite difference method for near-edge structure) and the excellent analysis of XANES (X-ray absorption near-edge structure) (Joly, 2001; Joly *et al.*, 1999) towards the analysis of XAFS using the finite difference method for XAFS (FDMX) (Bourke *et al.*, 2007).

The reliability of XAS depends upon the reliability of intensity measurements and the calibration of the energy scale using calibrated detectors for transmission or fluorescence modes (Diaz-Moreno, 2012). In addition, the stability of the X-ray energy and statistical accuracy are crucial for accurate determination of interatomic distances (Pettifer *et al.*, 2005). For retrieving structural features including the treatment of molecular vibrations from gaseous hydrides, an independent measure of the atomic background is required (Prešeren *et al.*, 2001). Solvent properties also affect the reactivity of metal complexes and their stability in solution. Characterization of solvent effects is important to quantify structural analysis of metal complexes in solution (Kurisaki *et al.*, 2008).

For structural analyses, fluorescence XAS, with precision obtained by multi-element detectors, is widely used for chemical, biological, environmental or organometallic materials, where only dilute solutions are available. A key advantage of fluorescence XAS is lower noise-to-signal ratio (Cramer *et al.*, 1988; Furenlid *et al.*, 1992) using appropriate regions of interest in a typical solid state detector. For this, the fluorescence detector must be equipped with energy-resolution low-pass filters, energy-resolving solid-state fluorescence detectors, multilayer diffraction gratings (Zhang *et al.*, 1998) or analysing monochromators, thereby providing higher resolution and lower signal-to-noise ratio (Jaklevic *et al.*, 1977; Goulon *et al.*, 1982). However, fluorescence measurements are typically performed on a relative scale of amplitude, and reliable uncertainties are usually not obtainable from experimental conditions. Sample concentration and the effective density of solution in the cell are typically unavailable, which limits both the absolute accuracy of attenuation and absorption coefficients but also limits the ability to determine the accuracy of derived parameters such as bond length and Debye broadening.

A key systematic with a fluorescence geometry multi-pixel system is the self-absorption effect (Pfalzer *et al.*, 1999). Amongst other systematics, sample thickness can distort the fluorescence XAS (Meitzner & Fischer, 2002), energy offset can provide misleading refinement, and harmonic contamination, dark current and scattering can affect the incident intensity I_0.

Transmission XAS is considered to be limited to solid and highly concentrated samples, and depends on the energy of the absorption edge of interest (Penner Hahn, 1999*a*,*b*). Transmission XAS can provide information for absolute measurements and error analysis from the characterization and correction of experimental systematics (Tran *et al.*, 2003), providing high-accuracy data and additional insight for reliable structural information. However, transmission XAS from dilute solutions is affected by high background attenuation (Jaklevic *et al.*, 1977), and therefore poor signal-to-background ratios. In either transmission or fluorescence, remarkable insight has been obtained in many detailed studies (Dau *et al.*, 2003; Cotelesage *et al.*, 2012). The opportunities with higher accuracy, higher precision and defined information content are perhaps obvious.

High fluxes at synchrotrons permit highly accurate measurements on absolute and relative scales using multiple solutions and solid samples by incorporating key protocols of the XERT (Chantler, 2010) with more standard XAS. To obtain XAS on an absolute scale with defined uncertainty, the technique must characterize experimental systematics of dark current, harmonic contamination, scattering and multipoint energy calibration.

2. The hybrid technique, and experimental details

We detail a new technique, the *hybrid technique*, for dilute systems and especially solutions, applied here to obtain absolute intensity and attenuation (transmission) measurements of the isomers bis(*N*-n-propyl-salicylaldiminato) nickel(II), (n-pr Ni), and bis(*N*-i-propyl-salicylaldiminato) nickel(II), (i-pr Ni), complexes. These (n-pr Ni) and (i-pr Ni) isomers have NiO_2N_2 geometries approximating square planar (Britton & Pignolet, 1989) and tetrahedral (Fox *et al.*, 1963, 1964), respectively. Highly accurate (<1% accuracy) absolute XAS will be used for investigating potential physical and chemical insight and their structural geometries based on reliable XAFS refinement statistics using the accuracy of the determined XAS. Hybrid XAS is expected to provide insight into metallic compounds including nickel(II) complex isomers and ferrocene (Chantler *et al.*, 2012).

The hybrid technique can be summarized as follows:

(i) Measurements are conducted on dilute homogeneous samples with parallel measurements on materials with differing absorber concentrations. The path-length of the sample is deduced from the solvent background absorption.

(ii) Accurate background solvent absorption measurements are conducted over an extended energy range. This requires correction for the air-path and attenuation due to the ion chamber and cryostat windows.

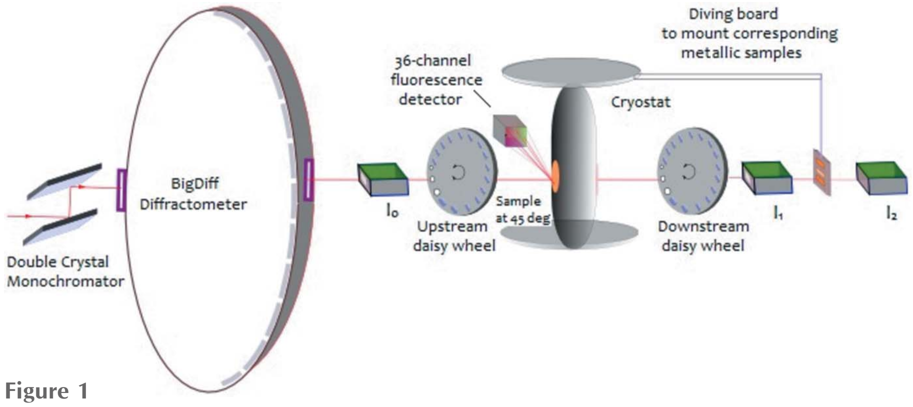

Figure 1
Schematic diagram of the experimental set-up using the hybrid technique at the ANBF, Tsukuba, Japan. A multi-chambered solution cell was used in the cryostat containing two dilute solutions and the pure solvent in three chambers. The cryostat is translated vertically to record intensities attenuated by each of the solutions at each energy. Two daisy wheels containing 14 aluminium filters (of different thicknesses) were employed upstream and downstream to monitor harmonic contamination for higher-order reflections. Different aperture sizes on the daisy wheel allowed aperture-dependent measurements to characterize the scattering effect for correction. Three ion-chambers were employed to record unattenuated intensities, I_0, attenuated intensities by the dilute solutions, I_1, and further attenuated by the corresponding metallic sample mounted with a cantilever as shown, I_2.

(iii) Simultaneous measurement of transmittance and fluorescence using ion chamber and multichannel fluorescence detection are possible. The sample is set at an angle near 45° to the X-ray beam, where the angle is obtained by modelling the self-absorption of the fluorescence signal on the fluorescence multichannel detector. The final accuracy may be based upon transmission and/or fluorescence data. Unlike more conventional XAS, transmission data are not used to define a single energy to perhaps 2–4 eV but rather to at least gain insight into the whole sample, geometry and scattering process.

(iv) The systematics associated with the experiment and X-ray beam such as harmonic contamination, scattering, energy calibration, detector dark current and self-absorption are characterized and corrected as has been established previously for XERT, though the methodology is different, especially for low-temperature systems including at liquid-helium temperatures.

It is commonly the case that a beamline cannot provide accurate energy characterization such as we use in XERT. The space and time for multiple thicknesses is usually not feasible or possible for dilute systems. Further, the statistical precision for a dilute system (solution) will necessarily be poor compared with an ideal reference foil, and signal-to-noise will be a potentially major issue. Many dilute systems are also photo-degraded in a powerful X-ray beam. In these cases the technique must be developed and hybridized with insights from other groups and researchers and indeed directly optimized for such solutions, cells and cryostat systems, as discussed here. One immediate consequence of these points is that the necessary statistical analysis required to determine uncertainty must be rewritten and rederived. Ideally the hybrid technique will become able to provide hybrid XAS (fluorescence and transmission XAS) of multiple materials (compound and element) by developing fluorescence XAS in line with XERT principles.

Fig. 1 shows a schematic experimental set-up at the ANBF (Tsukuba, Japan) using the hybrid technique to collect transmission and fluorescence XAS from multiple dilute solutions of nickel(II) complexes, and absorption spectra from a corresponding 5 µm Ni foil. To obtain consistent measurements at each energy with each of the solutions, it was necessary to develop a multi-chambered solution cell suitable for cryostat use.

Selection of the different samples was achieved by a *Y*-axis translation of the cryostat. Two daisy wheels, each of which contained 14 aluminium filters (with different thicknesses) along its perimeter, were located upstream and downstream of the X-ray beam to monitor harmonic contaminations as measured from thickness-dependent measurements. In addition, aperture-dependent measurements were made using three different-sized apertures on each of the daisy wheels to quantify the scattering effect on the measurements for their corrections. The BigDiff diffractometer installed at the ANBF was used for energy calibration following the powder diffraction method (Tantau *et al.*, 2014).

The three types of measurements, with multiple solutions (fluorescence and transmission) and with the corresponding metallic sample (absorption), were performed in two consecutive stages employing three ion chambers and a fluorescence detector as shown in Fig. 1. In the first stage, simultaneous transmission and fluorescence measurements were made with the multiple solutions in the cryostat. Secondary absorption measurements were performed in the second stage with a reference 5 µm-thick nickel foil at room temperature using a cantilever-mounted solid sample, in order to give a weak single-energy calibration reference. As seen in the analysis below, the use of a purpose-built energy measurement tool such as BigDiff or some other scanning analyser provides much higher accuracy in almost all cases. Among the three ion chambers, the first ion chamber recorded the unattenuated X-ray intensity I_0 before the beam is incident on the solutions. The second ion chamber recorded intensities I_1 attenuated by the solution cells. The third ion chamber recorded the intensity attenuated further by the metallic sample mounted onto a cantilever fixed to the cryostat and located between I_1 and I_2 (Fig. 1). The intensities at the second ion chamber acted as unattenuated intensities for the metallic sample.

2.1. Samples and sample properties

Solutions of differing concentrations (15 m*M* and 1.5 m*M*) for each of the complex isomers (Table 1), together with a mixed solvent (used to prepare the solutions), were loaded into the sample compartments for both transmission and

Table 1
Samples used in the experiment.

This paper reports results using data from run 1 (i-pr Ni) and run 2 (n-pr Ni) nickel(II) isomers. The order of solutions listed indicates the sample position (top, middle, bottom).

Run	Solution (m*M*)	Temperature (K)	Room-temperature reference sample
Run 1 (i-pr Ni)	15, solvent, 1.5	15	5 µm Ni foil, Cu foil
Run 2 (n-pr Ni)	Solvent, 1.5, 15	15	5 µm Ni foil, Cu foil

fluorescence measurements in the cryostat, and a 5 µm-thick metallic nickel foil was used for secondary absorption measurements at room temperature. A mixed solvent of 60% butyronitrile (BCN) + 40% acetonitrile (ACN) was used to prepare the solutions to avoid microcrystallization at low temperatures in the cryostat.

For the (i-pr Ni) isomer, we used 0.1462 g of solute in a 25 ml volumetric flask measuring 19.93 g of 15.30 m*M* solution, which was then diluted to obtain a 1.52 m*M* solution as the diluted solution. For the (n-pr Ni) isomer, we used 15.32 m*M* and 1.54 m*M* solutions for the measurements in the second run. Three prepared solutions were then filled into the chambers of the cell mounted onto a cryostat stick, and then frozen using liquid N_2 before placing into the cryostat for measurements. However, the density (ρ) and path-length (ρt) of a given solution are changed significantly at low temperatures (15–140 K) in the cryostat. Accurate measurement of sample properties and the density of the frozen solution were needed to characterize the solvent effect and for separating from the solution attenuation. This is particularly important for absolute X-ray attenuation measurements from solution with determination of systematic uncertainty, which is a key objective of the hybrid measurements.

To determine the density of the frozen solvent, a simple experiment was performed recording the changes in volume of the BCN/ACN solvent in liquid N_2 using a measuring cylinder. A quantity of 9 ml pure solvent was measured using a burette at room temperature and transferred to a measuring cylinder, which was then covered to prevent evaporation. The measuring cylinder with the solvent was cooled to liquid-N_2 temperature and the final volume of the solvent was measured at about 80 K. Repeated measurements were made to determine the uncertainty of the change in volume. Upon freezing to liquid-N_2 temperatures, a 21.5% decrease in volume was found; hence, the density of the frozen solvent was 0.9485 ± 0.0045 g ml^{-1}. The uncertainty in density ρ was determined from the uncertainty of the mass m and the volume V measurements. The density of the solvent allowed the determination of the path-length $[\rho t]_{\rm SV}$ of the pure solvent and other frozen solutions where the thicknesses of the solution chambers and the quantities of the samples were known.

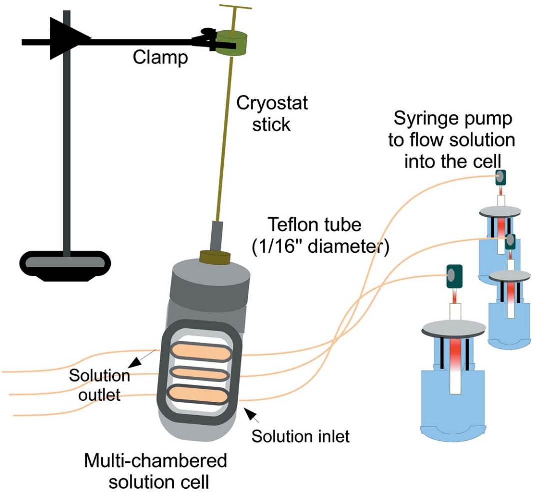

Figure 2
A three-chambered cryostat cell is filled with three solutions [15 m*M*, 1.5 m*M* nickel(II) complex and pure solvent]. A precise flow of solution into the chambers was achieved using three 10 ml syringe pumps, with fittings, and 1/16″ Teflon tubes. The cell, mounted on a cryostat stick, was clamped in the horizontal plane. Each syringe pump was controlled by a stepper-motor controller programmed by software to pulse the syringe pumps.

2.2. Multi-chambered solution cell, and its operation

In order to apply the hybrid technique to samples held at cryogenic temperatures, as necessary to minimize the effects of photoreduction, it is necessary to construct a compact sample cell that can contain a minimum of three samples in an area able to be addressed through the window of the cryostat. Moreover, it is important that the sample holder itself does not attenuate or clip the fluorescent photons detected using the multichannel detector. The solution cells were fashioned from a 25 mm-diameter by 2 mm Teflon pellet with a central 1.5 mm × 14 mm slot with 2 mm × 14 mm slots 2 mm above and below the central slot. The chambers were designed with dimensions to allow an X-ray beam of 1.5 mm × 2 mm size to pass through. The front and back windows of the cell were formed from Kapton adhesive tape pressed against the Teflon pellet by slotted aluminium plates aligned with the slots in the Teflon disc. The aluminium slots were chamfered to maximize the unimpeded optical path. A light film of silicone grease applied to the front and back surfaces of the Teflon disc improved the seal to the Kapton windows and minimized the risk of solutions leaking between chambers. The sample solution was flowed into the cell using 1/16″ Teflon tubing which was press-sealed on either side of the slot.

In operation it was found to be extremely important to maintain a steady flow of solution into the cells simultaneously to minimize pressure between adjacent slots. Control of solution flow was achieved using computer-controlled syringe pumps. After simultaneously filling the three sample slots, the syringe pumps were stopped and the sample cell immersed in liquid nitrogen. Once the sample had equilibrated at 80 K, the Teflon tubing was removed from the sample holder and the sample was then in a form suitable for loading into the beamline cryostat. Filling of the chambers is illustrated in Fig. 2.

3. Analysis

This analysis used measured intensities I and I_0 from two separate runs with two isomers, (i-pr Ni) and (n-pr Ni), where the measurements were made using three solutions (including two concentrations and their corresponding solvent) for each of the isomers. Simultaneous intensity measurements using a 5 µm-thick nickel foil allowed a calibration of the solution spectra. For characterizing experimental systematics for their correction, data on key experimental systematics including energy calibration, dark current, harmonic contamination (Islam *et al.*, 2014) and scattering (Tran *et al.*, 2003) were also collected. Dark current was recorded at each of the energies in both upstream and downstream ion-chambers, and then fitted with respect to counting time. Recorded intensities (I_0, I) were normalized by subtracting the fitted dark currents to remove the non-linearity of this particular systematic. Attenuation of all three solutions including the solvent was then determined using dark-current-corrected intensities.

Table 2
Measured quantities of nickel(II) complex isomers for the solution samples used for the measurements.

The density of the pure solvent (used to prepare the solutions) was measured in liquid nitrogen as detailed in §2.1.

Sample nickel(II) complex isomers	Mass fraction (*w*/*w*)	% uncertainty of fraction	Molarity (m*M*)	% uncertainty of molarity	Temperature (K)
(i-pr Ni)	0.007336 ± 0.000003	0.04	15.26 ± 0.03	0.2	295 ± 1
(i-pr Ni)	0.0007281 ± 0.0000023	0.31	1.515 ± 0.006	0.4	295 ± 1
(n-pr Ni)	0.007469 ± 0.000031	0.41	15.33 ± 0.06	0.4	297 ± 1
(n-pr Ni)	0.0007508 ± 0.0000032	0.43	1.541 ± 0.006	0.4	297 ± 1

Solvents	Density (g ml^{-1})	Temperature (K)
CH_3CN (ACN)	0.7769 ± 0.0008	–
C_2H_7CN (BCN)	0.784 ± 0.001	–
Mixed solvent	0.781 ± 0.001	296 ± 1
Mixed solvent (frozen)	0.9485 ± 0.0045	63–77

The next step of this analysis was the characterization of background contributions to the determined attenuations of the solutions for removing this systematic effect. To determine the accurate path-length $[\rho t]_{\rm SV}$ of the pure solvent, we modelled the attenuations of the identified background absorbers, detailed in §3.2.1. The background absorbers were modelled using the experimental geometry and tabulated data of X-ray mass attenuation coefficients of the absorbers (FFAST; Chantler, 2000). Following modelling of the background attenuation, the other systematics including energy calibration, harmonic contamination and scattering effect were characterized and corrected for sample attenuations (Table 2).

3.1. Attenuations of the isomers and the pure solvent

Recorded intensities were first normalized to recorded dark currents (when there is no beam an ion chamber records some counts subject to the low-count-rate linearity of the detector) to determine the solution attenuations. Attenuations of the solutions including the solvent were determined from the dark-current-corrected intensities using equation (1) and the corresponding uncertainty using equation (8).

The Beer–Lambert equation must be corrected for dark-current readings using

$$\left[\frac{\mu}{\rho}\right][\rho t] = -\ln\left(\frac{I-D}{I_0-D_0}\right), \tag{1}$$

and for detector normalization following XERT as follows,

$$\left[\frac{\mu}{\rho}\right][\rho t] = -\ln\left[\left(\frac{I-D}{I_0-D_0}\right)\Big/\left(\frac{I-D}{I_0-D_0}\right)_{\rm blank}\right], \tag{2}$$

where I and I_0 are the attenuated and unattenuated intensities, and D and D_0 are the recorded dark-currents in the detector and monitor, respectively. In XERT, the blank measurements are those with a foil or sample absent, so that all attenuation from detectors, air-path and Kapton or beryllium windows, for example, are excluded and the measurement is solely related to the sample. The normalization corrects for differential amplification of the upstream and downstream detectors. However, for dilute systems, especially with a dominant solvent signature, attenuation (transmission) measurements have a large background signal with a smooth but structured character. Since we are interested in the active site of the dilute system in the solvent, and not the solvent matrix, we must redefine the blank measurement to be that of the (pure) solvent:

$$\left[\frac{\mu}{\rho}\right][\rho t] = -\ln\left[\left(\frac{I-D}{I_0-D_0}\right)\Big/\left(\frac{I-D}{I_0-D_0}\right)_{\rm solvent}\right], \tag{3}$$

$$\left[\frac{\mu}{\rho}\right][\rho t] = -\ln\left(\frac{I-D}{I_0-D_0}\right) + \ln\left(\frac{I-D}{I_0-D_0}\right)_{\rm solvent}, \tag{4}$$

or, perhaps more simply,

$$\left[\frac{\mu}{\rho}\right][\rho t]_{\rm S} = \left[\frac{\mu}{\rho}\right][\rho t]_{\rm S+SV+BKG} - \left[\frac{\mu}{\rho}\right][\rho t]_{\rm SV+BKG}, \tag{5}$$

where the subscripts S, SV and BKG refer to the solute (in solution), pure solvent and the background absorbers (including air-path, window materials, detector and cryostat gas). Simultaneous measurement of the incident and transmitted intensities should normalize any intensity fluctuation in the measured attenuation. This method also normalizes differences in efficiency and electronic gain between the ion chambers.

Dark-current-corrected attenuations are shown in Figs. 3 and 4. The quality of the collected data is represented by the percentage uncertainty presented in the plots underneath. Clearly, there is a variation in background levels between the collected spectra, which is due to path-length variations for the

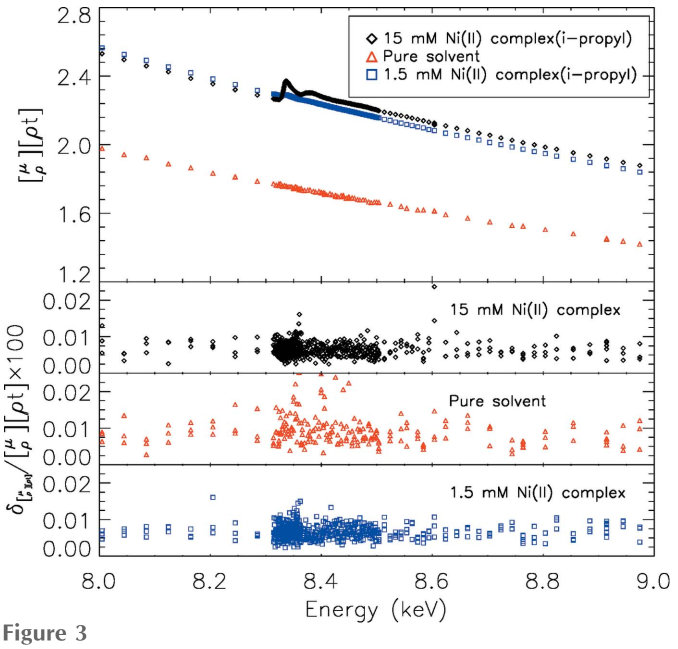

Figure 3

Determined X-ray absorption spectra and corresponding uncertainties using two solutions (15 m*M* and 1.5 m*M*) of the (i-pr Ni) complex, and the pure solvent (#1, #2, #3; Table 3). Equations (1) and (8) were used to determine the spectra and the corresponding uncertainty. The black diamond markers represent the measurements with the 15 m*M* solution, and the measurements with the 1.5 m*M* solution and the pure solvent are represented by the blue square markers and the red triangles, respectively. The percentage uncertainties are represented by the plots underneath using the corresponding coloured markers for the solution spectra. A 0.005–0.06% variation in the uncertainties over the energy range represents the quality of data from the solutions. Clearly, there was background variation between the spectra, which is mainly contributed to by the variation in effective density $[m/A]_{\rm eff}$ of the solutions in different chambers. The well defined peaks confirm that there was negligible leaking between the solutions through the chambers. From the spectra it is, however, clear that the pure solvent had not uniformly filled the sample compartment in the frozen sample, causing a linear offset from the background of the solutions. Modelling of the solvent (using the known experimental geometry) can quantify and correct for this significant background effect.

solution chamber path-lengths, and solution flow into the cell (§3.2). The quantity on the left-hand side of equation (2) represents the attenuation of all the matter between the front sides of the upstream and the downstream ion chambers. To determine the attenuation of the solute (in solution) alone, three measurements were made, two with dilute solutions (15 m*M* and 1.5 m*M*) and one with the pure solvent used to prepare the solutions.

Characterization of solute attenuation from dilute solutions is complicated by the significant background attenuation contributed by the pure solvent and other background absorbers that exist between the monitor and the detector. To obtain XAS on an absolute scale, we must model the background attenuation by the pure solvent and by other absorbers. This allows the determination of accurate path-length $t_{\rm SV}$ or integrated column densities $[\rho t]_{\rm SV}$ of the pure solvent for determining XAS of the solute on an absolute scale as detailed in the following sections.

Although the solutions were contained in the chambers with the same nominal path-lengths t, there were still background variations between the spectra of the solutions (§3.2). The X-ray mass attenuation coefficients $[\mu/\rho]$ of the solutions can then be determined by measuring or fitting the path-lengths and normalizing,

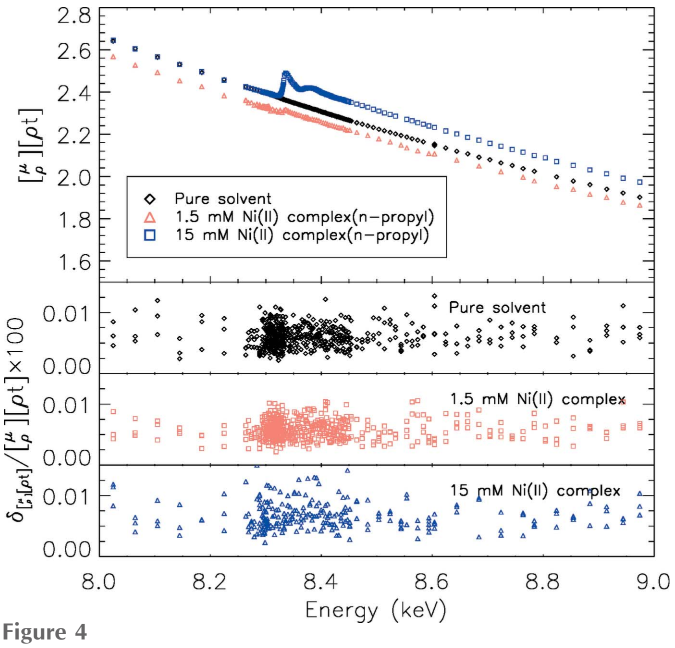

Figure 4

X-ray absorption spectra using two solutions (15 m*M*, 1.5 m*M*) with the (n-pr Ni) complex and the pure solvent used to prepare the solutions (rows #4, #5, #6; Table 3). Equations (1) and (8) were used to determine the spectra and the corresponding uncertainty or the independent quality of the data. As in Fig. 3, the corresponding uncertainties are presented in the plots underneath using the same markers and colours for the corresponding solutions. Compared with the obtained spectra with the tetrahedral (i-pr Ni) complex, the variation between the backgrounds of the spectra for the square planar (n-pr Ni) complex are quite minor. To model the solvent attenuation for subtraction the solvent absorption represented by the black diamonds was used and subtracted from the solution absorption.

$$\left[\frac{\mu}{\rho}\right][\rho t]_{\rm S} = -\ln\left(\frac{I-D}{I_0-D_0}\right) + t_{\rm ratio}\ln\left(\frac{I-D}{I_0-D_0}\right)_{\rm solvent};$$
$$t_{\rm ratio} = \frac{t}{t_{\rm solvent}}. \tag{6}$$

This equation assumes that the solvent contributions and path-length SV are dominant over the incidental backgrounds BKG. If the contributions from BKG can be defined and subtracted separately, then the scaling for the SV component is then

$$\begin{aligned}\left[\frac{\mu}{\rho}\right][\rho t]_{\rm S} &= -\ln\left(\frac{I-D}{I_0-D_0}\right) + \frac{t}{t_{\rm SV}}\ln\left(\frac{I-D}{I_0-D_0}\right)_{\rm SV} \\ &\quad + \ln\left(\frac{I-D}{I_0-D_0}\right)_{\rm BKG} \\ &= -\ln\left(\frac{I-D}{I_0-D_0}\right) + t_{\rm ratio}\ln\left(\frac{I-D}{I_0-D_0}\right)_{\rm SV} \\ &\quad - \left[\frac{\mu}{\rho}\right][\rho t]_{\rm BKG};\end{aligned}$$
$$t_{\rm ratio} = \frac{t}{t_{\rm SV}}. \tag{7}$$

The uncertainty propagation is a little complicated. Considering first the actual solution measurement [equation (1)], we have

$$\delta_{[\frac{\mu}{\rho}][\rho t]} = \left[\frac{\delta^2\left(\frac{I-D}{I_0-D_0}\right)}{\left(\frac{I-D}{I_0-D_0}\right)^2} + \frac{\delta_D^2}{(I-D)^2} + \frac{\delta_{D_0}^2}{(I_0-D_0)^2} \right]^{1/2}. \tag{8}$$

Fractional (or percentage) uncertainties in I/I_0 become absolute uncertainties in the logarithm. We assume here that the uncertainties in the overall ratio are decoupled from those of each of the dark currents (detector noise).

The variance of the ratio is normally accomplished by the variance in the repeated (ten or so) measurements of each ratio, after correction for dark currents in the detectors. This assumes high correlation between the upstream signal I (or $I - D$) and the downstream signal I_0 or $I_0 - D_0$. If the signals are uncorrelated or negatively correlated (as does sometimes occur), then statistical analysis would require that the variance be determined from the variance of the numerator and denominator separately. An error of D or D_0 contributes to the observed variance of the ratio; so that even if these parameters are quite uncorrelated in measurement, they are partially correlated in this propagation. However, this prescription gives a reliable overestimate of the standard error.

Developing the prescription now to include the normalizing solvent measurements ideally, as per equations (4) or (5), and assuming that the solvent measurements are uncorrelated with the solution measurement, we have

$$\begin{aligned} \delta^2_{[\frac{\mu}{\rho}][\rho t]_{\rm S}} = {} & \left[\frac{\delta^2\left(\frac{I-D}{I_0-D_0}\right)}{\left(\frac{I-D}{I_0-D_0}\right)^2} \right] + \left[\frac{\delta^2\left(\frac{I-D}{I_0-D_0}\right)}{\left(\frac{I-D}{I_0-D_0}\right)^2} \right]_{\rm solvent} \\ & + \delta_D^2 \left[\frac{1}{(I-D)} - \frac{1}{(I-D)_{\rm solvent}} \right]^2 \\ & + \delta_{D_0}^2 \left[\frac{1}{(I_0-D_0)} - \frac{1}{(I_0-D_0)_{\rm solvent}} \right]^2. \end{aligned} \tag{9}$$

Including the correction for solvent path-length compared with that of the sample path-length, as given in equation (6), yields

$$\begin{aligned} \delta^2_{[\frac{\mu}{\rho}][\rho t]_{\rm S}} = {} & \left[\frac{\delta^2\left(\frac{I-D}{I_0-D_0}\right)}{\left(\frac{I-D}{I_0-D_0}\right)^2} \right] + \left[\frac{\delta^2\left(\frac{I-D}{I_0-D_0}\right)}{\left(\frac{I-D}{I_0-D_0}\right)^2} \right]_{\rm solvent} \\ & + \delta^2(t_{\rm ratio}) \ln^2\left(\frac{I-D}{I_0-D_0}\right)_{\rm solvent} \\ & + \delta_D^2 \left[\frac{1}{(I-D)} - \frac{1}{(I-D)_{\rm solvent}} \right]^2 \\ & + \delta_{D_0}^2 \left[\frac{1}{(I_0-D_0)} - \frac{1}{(I_0-D_0)_{\rm solvent}} \right]^2. \end{aligned} \tag{10}$$

If the solvent and solution measurements have the same values of I and $I_{\rm solvent}$ then the error from the dark current effectively cancels. We expect that the upstream measurements I_0 and $(I_0)_{\rm solvent}$ will obey this so that the last term is likely to be insignificant. Further, with suitable amplification, $I_0 \gg D_0$, so that the contribution of the last term in either error propagation is likely to be small and insignificant. For high absorption, however, I and D could be similar, so that this component could make a large contribution in the error analysis following equation (8) or a relatively small contribution following equation (9). Finally, inclusion of the separation of the solvent contribution from background contributions in transmission as per equation (7) yields the final equation,

$$\begin{aligned} \delta^2_{[\frac{\mu}{\rho}][\rho t]_{\rm S}} = {} & \left[\frac{\delta^2\left(\frac{I-D}{I_0-D_0}\right)}{\left(\frac{I-D}{I_0-D_0}\right)^2} \right] + \left[\frac{\delta^2\left(\frac{I-D}{I_0-D_0}\right)}{\left(\frac{I-D}{I_0-D_0}\right)^2} \right]_{\rm SV+BKG} + \delta^2_{[\frac{\mu}{\rho}][\rho t]_{\rm BKG}} \\ & + \delta^2(t_{\rm ratio}) \ln^2\left(\frac{I-D}{I_0-D_0}\right)_{\rm SV} \\ & + \delta_D^2 \left[\frac{1}{(I-D)} - \frac{1}{(I-D)_{\rm SV+BKG}} \right]^2 \\ & + \delta_{D_0}^2 \left[\frac{1}{(I_0-D_0)} - \frac{1}{(I_0-D_0)_{\rm SV+BKG}} \right]^2. \end{aligned} \tag{11}$$

3.2. Path-lengths for the frozen solutions and variation between spectra

The attenuation of the pure solvent and other background absorbers has been determined with high accuracy to remove their effect from the spectra. This was made possible by collecting direct measurements with the pure solvent used to prepare the solutions, tabulated data of X-ray mass attenuation coefficients of the absorbers (FFAST; Chantler, 2000) and the experimental geometry measured from the actual experimental set-up (Fig. 5). The experimental geometry provided

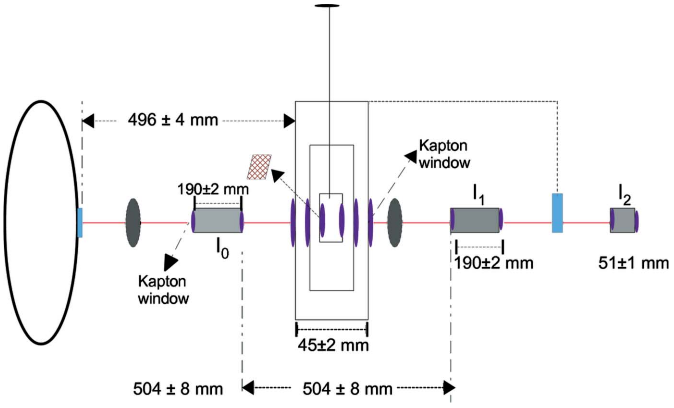

Figure 5
Geometry of the experiment performed to collect XAS data in this analysis. This provides the path-lengths of the identified background absorbers responsible for the thick background of the XAS from dilute solutions.

Table 3
Path lengths of the three-chambered solution cell used for the measurements, and derived parameters related to the chambers using the attenuations of the solutions.

The second column lists the samples and solution concentrations used in the measurements for each of two runs. The third column lists the positions of the solutions in the chambers, where two different cells (mechanically with the same geometries and chambers' path-lengths) were used in two different runs. Measured (using a micrometer) path-lengths of the solutions are listed in the fourth column, where the path-lengths were found to vary by −0.05% to 0.3% based upon the micrometer measurements. The fifth column lists the densities of the frozen solutions determined by combining the solvent density with the density of the solutes (m/V) (g ml^{-1}) used for preparing the corresponding concentrations [*i.e.* for 15 m*M* (i-pr Ni) solution, solute density = 0.1462/25 g ml^{-1}; $\rho_{\rm SLN} = \rho_{\rm SV} + \rho_{\rm solute}$]. The sixth column determines the nominal column densities $[\rho t]_{\rm NOM}$ of the samples by multiplying the densities of the solutions with the spacers' nominal path-lengths or thicknesses taking account of the chambers' angular positions at 45°. The seventh column lists the attenuations of the solutions at particular energies (8.8 keV and 8.82 keV for two different runs) used to determine the column densities $[\rho t]_{\rm SV+BKG}$ of the solutions including the background contributions. The eighth column lists $[\mu/\rho]_{\rm FFAST}$ of the solvent using tabulated data of X-ray mass attenuation coefficients (FFAST; Chantler, 2000), where the attenuations of the solutions were divided by $[\mu/\rho]_{\rm FFAST}$ to obtain the column densities of the solutions listed in the ninth column. The tenth column lists the ratios of the nominal path-lengths $[\rho t]_{\rm NOM}$ to the measured path-lengths $[\rho t]_{\rm SV+BKG}$ indicating the significant contributions by the background attenuations, which further exaggerates the path-length variations.

	Sample nickel(II) complex	Sample position	Nominal path-length (mm)	Density (g ml^{-1})	$[\rho t]_{\rm NOM}$ (g cm^{-2}), B	$[\mu/\rho][\rho t]_{\rm SV+BKG}$	$[\mu/\rho]$ (cm^2 g^{-1}) solvent	$[\rho t]_{\rm SV+BKG}$ (g cm^{-2}), A	Ratio (SV+BKG)/NOM, A/B
						(at 8.8 keV)	(at 8.8 keV)		
#1	15 m*M* (i-pr Ni)	Top (−4.5)	1.9577 ± 0.0017	0.9543 ± 0.0068	0.2642	1.985 ± 0.0001		0.5515	2.0873
#2	Pure solvent (0.6BCN + 0.4ACN)	Middle (0)	1.9567 ± 0.0014	0.9485 ± 0.0045	0.2625	1.505 ± 0.0001	3.599	0.4182	1.5933
#3	1.5 m*M* (i-pr Ni)	Bottom (4.5)	1.9517 ± 0.0013	0.9491 ± 0.0103	0.2620	1.948 ± 0.0001		0.5413	2.0664
						(at 8.82 keV)	(at 8.82 keV)		
#4	Pure solvent (0.6BCN + 0.4ACN)	Top (−4.5)	1.9742 ± 0.0017	0.9485 ± 0.0045	0.2648	1.998 ± 0.0001		0.5589	2.1105
#5	1.5 m*M* (n-pr Ni)	Middle (0)	1.9783 ± 0.0018	0.9491 ± 0.0110	0.2655	1.952 ± 0.0001	3.575	0.5460	2.0563
#6	15 m*M* (n-pr Ni)	Bottom (4.5)	1.981 ± 0.002	0.9544 ± 0.0112	0.2674	2.070 ± 0.0001		0.5790	2.1655

the path-lengths or distances travelled by the identified absorbers, including the air-path, detector and cryostat windows, between the monitor and the detector as listed in Tables 3 and 4. Fig. 6 shows the modelled absorbers, and the fitted model of the solvent representing an excellent fit. This model allows for the determination of the accurate solvent and BKG path-lengths and separating them from that of the solute as required.

Densities of the background absorbers were used from the literature (third column in Table 4), and the density 0.9485 ± 0.0045 g ml^{-1} of the pure solvent (40% CH_3CN + 60% CH_3CH_2CN) at liquid N_2 temperatures. The attenuation contributed only by the solvent separated from the contribution of the BKG absorbers is determined by fitting the pure solvent path-length using the solvent model given in equation (12). This model can be used to fit the path-length of any individual BKG if not well estimated,

$$-\ln(I/I_0)_{\rm T} = \left[\frac{\mu}{\rho}\right]_{\rm SV}[\rho t]_{\rm SV} + \left[\frac{\mu}{\rho}\right]_{\rm N_2}[\rho t]_{\rm N_2} + \left[\frac{\mu}{\rho}\right]_{\rm air}[\rho t]_{\rm air} + \left[\frac{\mu}{\rho}\right]_{\rm Ne}[\rho t]_{\rm Ne} + \left[\frac{\mu}{\rho}\right]_{\rm w}[\rho t]_{\rm w}. \quad (12)$$

3.2.1. Separating solvent from the BKG absorbers and determining $t_{\rm ratio}$.

A significant variation between the solvent attenuation (with the pure solvent) and the attenuations of the solutions was found, due to slight path-length variations among the chambers from mechanical construction and incomplete filling of the sample compartment by the solvent which is not easily diagnosed at the time of the measurement. This leads to the requirement to determine $t_{\rm ratio}$ by fitting the path-lengths [using a solvent model, equation (12)] of the pure solvent and of the background of the sample attenuations (with a multi-chambered solution cell). To fit the background

Table 4
Estimated attenuation contributions by the background absorbers using theoretical data of X-ray mass attenuation coefficients (FFAST; Chantler, 2000), and the geometry of the experimental set-up as shown in Fig. 5.

The path-lengths of the identified matter between the monitor and the detector were determined from the measured geometry of the experimental set-up. Attenuation of the materials was then determined by multiplying the path-lengths by tabulated $[\mu/\rho]$ data.

Background absorber	Chemical formula	Density (g cm^{-3})	Path-length (cm)	$[\rho t]_{\rm NOM}$ (g cm^{-2})	$[\mu/\rho]_{\rm FFAST}$ (cm^2 g^{-1})	$[\mu/\rho][\rho t]_{\rm FFAST}$ (8.854 keV)
Air	N_2(78%) + O_2(21%) + Ar(0.93%)	0.0011	45.9 ± 0.6	0.05049	6.0214	0.3040
Detector gas	N_2	0.0012	19.0 ± 0.2	0.0228	5.372	0.1225
Kapton (polymide)	$C_{12}H_{10}N_2O_5$	1.42	0.02	0.03	4.8968	0.1126
Silicone (adhesive)	$CH_3Si_2O_2C_4H_9$	0.968	0.012	0.0116	23.3541	0.6773
Helium gas (cryostat)	He	0.0001785	2.2	0.0004	0.25578	0.0001

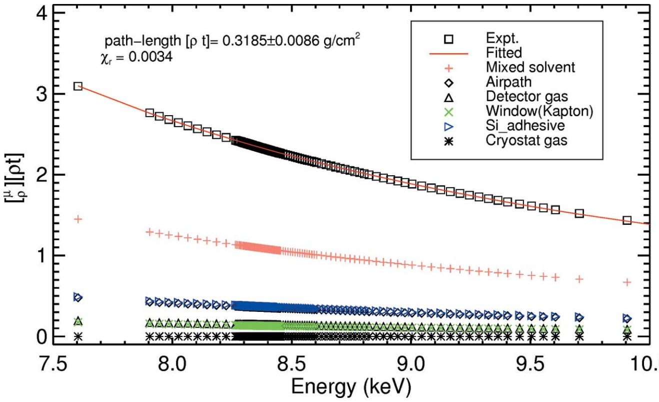

Figure 6
Fitting solvent background (#4, Table 3). Modelled attenuation of the background absorbers using the experimental geometry and respective densities. The path-length of two layers of silicone adhesive used on the Kapton windows was fitted, while attenuations of all other identified absorbers were in good agreement with their estimated values. An excellent fit was obtained for the solvent path-length required to determine the accuracy of the XAS from the solutions. Interestingly, the data could easily distinguish between errors of one component of the background path compared with another, despite all representing smooth and largely featureless curves. The slopes and curvatures are significantly different. The final XAS of the isomers were determined by dividing the attenuations $[\mu/\rho][\rho t]$ by the path-length $[\rho t]_{\rm SV}$. This allows estimation of accurate uncertainty $\sigma_{\mu t}/[\rho t]_{\rm SV}$ of the absolute XAS.

path-length of the sample attenuations, data were used at selected energies from the pre-edge, and far from the edge, avoiding the oscillatory regions. The background of the solution spectra was then scaled and normalized to an offset as modelled using the tabulated data of X-ray mass attenuation coefficients (FFAST; Chantler, 2000) of the nickel(II) complexes for relevant concentrations. We then fitted the path-length of the background (shown by the red solid line in Fig. 7) with solution XAS, and the path-length of the pure solvent attenuation. Therefore, the ratio $t_{\rm ratio}$ of the fitted path-lengths of the pure solvents was determined from the XAS with the pure solvent, and the XAS with the solution. The corresponding uncertainty was determined following a χ^2_r minimization to obtain the best fit.

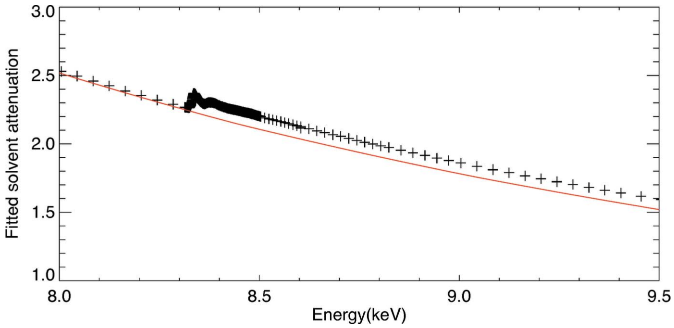

Figure 7
Method for normalizing and removing the solvent background. Determined XAS from 15 m*M* solution of (i-pr Ni), where the red solid line is the determined background by fitting the solvent path-length using a solvent model. The solvent model allows the determination of the path-length of the pure solvent (and other absorber) allowing the separation of the contributions by the solvent and by other background absorbers. The XAS from the solute only (quantity of substance in solution) was then determined by subtracting the background

For each of the samples (#1, #3, #5, #6) we followed the same procedure to determine accurate background to subtract from the sample attenuations. The X-ray attenuation $[\mu/\rho][\rho t]_{\rm S}$ of the isomers was then determined using equation (7). The path-length of one of the identified background absorbers (silicone-like absorber) was fitted as shown in Fig. 7. The solvent path-length was then fitted by constraining the path-lengths of other absorbers and the resulting path-length of the silicone-like absorber. This allows the separation of the background and the pure solvent contributions to the attenuations of the solution samples.

To model the background attenuations of the identified absorbers, tabulated data of X-ray mass attenuation coefficients of the absorbers including air-path, detector gas, cryostat gas, multiple Kapton tapes used as the detector, cryostat and (solution) cell windows were used (FFAST; Chantler, 2000). The path-lengths of the absorbers were determined from the experimental geometry shown in Fig. 5 and their respective densities. The thicknesses of the absorbers travelled by the X-ray beam between the monitor and the detector were multiplied by the respective densities of the absorbers to determined their path-lengths. Required densities of the background absorbers were used from the literature as listed in Table 4, and the density of the pure solvent in the frozen state was found to be 0.9485 ± 0.0045 g ml^{-1}.

The nominal column density $[\rho t]_{\rm NOM}$ of the pure solvent was first determined by multiplying the nominal path-length t of the solution chamber by the density $\rho(N_2)$ of the frozen solvent (Table 3) for modelling the background attenuations to the XAS, and thereby determining the accurate path-length $[\rho t]_{\rm SV}$ of the pure solvent. The nominal column density $[\rho t]_{\rm SV+BKG}$ of the mixed solvent was determined using

$$[\rho t] = \frac{[\mu/\rho][\rho t]_{\rm expt}}{[\mu/\rho]_{\rm theory}}, \tag{13}$$

where $[\mu/\rho][\rho t]_{\rm expt}$ is the attenuation of the pure solvent at a given energy, and $[\mu/\rho]_{\rm theory}$ is the theoretical (FFAST) X-ray mass attenuation coefficient of the solvent at that energy.

For the measurements with the (i-pr Ni) complex (run 1), $[\rho t]_{\rm SV+BKG}$ with the pure solvent (middle chamber) was found to be 0.4182 g cm^{-2} (using attenuation data) at 8.8 keV, which is much larger than the nominal column density $[\rho t]_{\rm NOM}$ = 0.2625 g cm^{-2}. For the measurements with the (n-pr Ni) isomer, the column density $[\rho t]_{\rm SV+BKG}$ was found to be larger compared with the measurements of (i-pr Ni) in run 1, as listed in Table 3.

3.3. Normalized attenuations $[\mu/\rho][\rho t]_{\rm S}$ of the complexes

Subtraction of the determined background attenuations from the total attenuations of the solutions provided the normalized XAS of the complexes using equation (7) as shown in Figs. 8 (i-pr Ni) and 9 (n-pr Ni). The corresponding uncertainty includes the variance of the repeated measurements with the sample and the solvent [parts 1 and 2 of equation

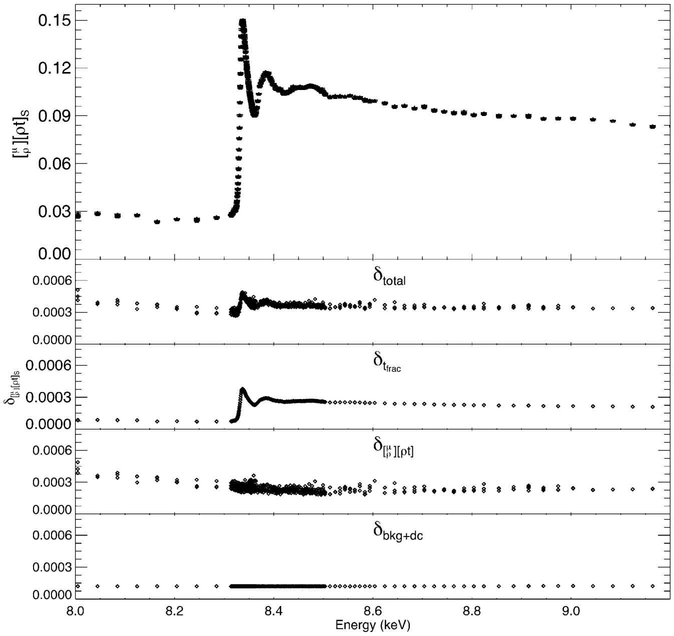

Figure 8
Corrected and normalized XAS of the (i-pr Ni) isomer determined from the attenuations of 15 m*M* solutions following the solvent subtraction as illustrated in Fig. 6. The modelled background (Fig. 6) was subtracted from the corrected (dark-current and scattering effect) attenuations of the solutions (shown in Fig. 3 by the diamond symbols; sample detail: #1, Table 3). The corresponding uncertainty was propagated from the uncertainty contributions of experimental systematics, and from the variance of repeated measurements with both the solution and the solvent. The defined accuracy will allow the reliable structural analysis of (i-pr Ni) using XAFS. At each of the energies, three aperture-dependent measurements are in excellent agreement.

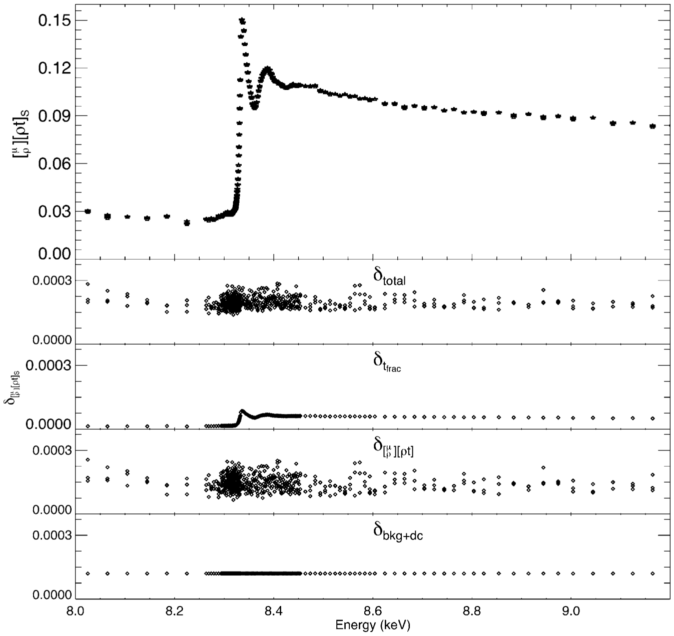

Figure 9
Corrected and normalized XAS of 15 m*M* (n-pr Ni) at the calibrated energies, with uncertainties from some of the key systematics including dark current, variance of the repeated measurements with both the solvent and the solution, thickness ratio, background attenuation, scattering effect and harmonic contamination. Three to six aperture-dependent measurements were made at each of the energies and are in excellent agreement. The determined uncertainty underneath shows the quality of data signifying the measurement accuracy. High-accuracy XAS for (n-pr Ni) was also obtained for the lower path-length fraction ($t_{\rm frac}$ = 0.9804 ± 0.0006).

(11)], absolute uncertainty in determining the path-length of the solvent and background (parts 3 and 4), and the correlated uncertainty from the dark-current measurements for both solvent and sample measurements (part 5 and 6).

Fitted path-lengths $[\rho t]_{\rm SLN}$ of the solutions were multiplied by their corresponding mass fractions $w_{\rm S}/w_{\rm SV}$ (listed in Table 2) to determine the absolute column densities of the complexes. The determined column densities were then used to determine the X-ray mass attenuation coefficients $[\mu/\rho]$ of the complexes by dividing the sample $[\mu/\rho][\rho t]_{\rm S}$ of the complexes by their integrated column densities $[\rho t]_{\rm S}$ following the correction of measurable experimental systematics detailed in §4.

3.4. Column densities $[\rho t]_{\rm S}$ of the isomers

Accurate determination of the path-lengths $[\rho t]_{\rm S}$ of the frozen solutions from the fitting procedure allowed the determination of the absolute integrated column densities $[\rho t]_{\rm S}$ of the samples (for the quantities in solutions). The fitted path-lengths $[\rho t]_{\rm S}$ of the samples were multiplied by their corresponding mass fractions w/w as listed in Table 2 to determine the absolute column densities, thereby determining the X-ray mass attenuation coefficients $[\mu/\rho]$ of the isomers by dividing the X-ray attenuations of the isomers by their integrated column densities as listed in Table 5.

The multiple measurements at each of the energies were in excellent agreement, and the final $[\mu/\rho][\rho t]_{\rm S}$ was determined from the weighted mean of the multiple measurements at each of the energies, and their weighted uncertainty was determined using their corresponding relative uncertainty as represented as error bars in Figs. 8 and 9.

4. Characterization of experimental systematics for their correction

Following the normalization of the solution attenuations to the solvent background, we characterized a number of other

Table 5
Fitted path-lengths of the frozen solutions, and the determined integrated column densities $[\rho t]_{\rm S}$ multiplying the path-lengths of the samples by their corresponding mass fractions used for preparing the solutions.

Samples	Mass fraction (w/w)	Path-length $[\rho t]_{\rm SLN}$	Column density $[\rho t]_{\rm S}$	% $\sigma_{[\rho t]_{\rm S}}$
#1 (i-pr Ni)	0.007336 ± 0.000003	0.25051 ± 0.00018	0.0018377(15)	0.08
#3 (i-pr Ni)	0.0007281 ± 0.0000023	0.26226 ± 0.00017	0.00019095(06)	0.32
#5 (n-pr Ni)	0.007469 ± 0.000031	0.25877 ± 0.00011	0.0019328(81)	0.41
#6 (n-pr Ni)	0.0007508 ± 0.0000032	0.24844 ± 0.00015	0.00018653(80)	0.43

systematics for their correction that included the path-length variation, harmonic contamination, scattering and the energy calibration. For the first time we have determined transmission XAS from solutions on an absolute scale, which were possible to characterize and correct for the systematics.

4.1. Path-length variation to multiple chambers of the solution cell

A solution cell with three chambers, each of depth 2 mm, provided the path-length of a given X-ray beam for absorption measurements. Micrometer measurements found that the path-lengths varied by 0.05–0.3% between the chambers due to their construction. The path-length of the middle chamber (used for solvent measurements) is 0.05% lower (about 1 µm) compared with that of the top chamber (used for measurements with a 15 m*M* solution), and 0.26% lower than that of the bottom chamber (used for measurements with a 1.5 m*M* solution).

The variation of the path-lengths between the chambers causes a background offset to the spectra collected in different chambers. Also, incomplete filling of the sample compartment causes a path-length variation for that particular chamber. For example, the spectra of the pure solvent shown in Fig. 3 by triangle markers varied significantly from the spectra of other solutions (of 15 m*M* and 1.5 m*M* concentrations), which is due to an incomplete filling of the solvent sample compartment. Two out of three chambers were filled with two solutions (15 m*M* and 1.5 m*M*) using two motor-controlled syringe pumps, and the middle chamber was filled with the pure solvent using a manually operated syringe. Manual operation has likely caused the middle chamber to have impacted on the reliability of the filling of the sample compartment.

Table 4 lists the path-lengths of the frozen solutions and the solvent determined using equation (12). The lower values of the solutions' nominal column densities $[\rho t]_{\rm NOM}$ compared with their experimental column densities $[\rho t]_{\rm SV+BKG}$ confirms that there was significant attenuation contributions from other background absorbers. This information was important for modelling the path-length $[\rho t]_{\rm SV}$ of the pure solvent for determining absolute uncertainties of the XAS from the solutions. For the measurements with (i-pr Ni) (run 1), $[\rho t]_{\rm SV+BKG}$ with the pure solvent (middle chamber) was found to be 0.4182 g cm^{-2} (using attenuation data) at 8.8 keV, which is much larger than the nominal column density $[\rho t]_{\rm NOM}$ = 0.2625 g cm^{-2}.

4.2. Scattering

The interaction between X-rays with energies around the *K*-edge and the frozen solutions can produce scattered photons. Two different-sized apertures located on the daisy wheels were used to observe the effect of scattering from the aperture-dependent measurements.

The difference between the aperture-dependent measurements was insignificant and no significant scattering effect was observed (Fig. 10). This is likely due to the matching of the upstream and downstream monitor and detector solid angles. Therefore no correction to the coefficients was required.

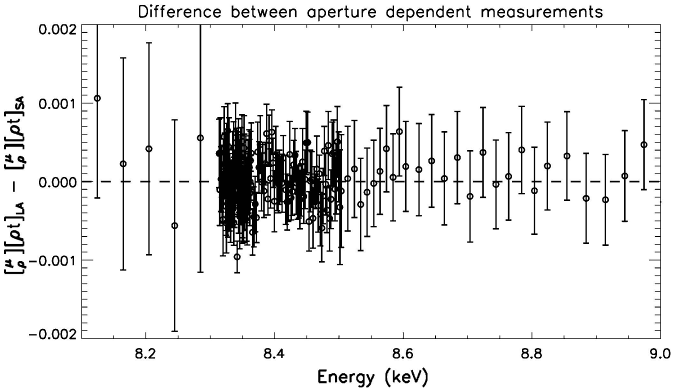

Figure 10
No significant scattering was observed from this analysis. Insignificant differences were observed from the aperture-dependent measurements.

4.3. Energy calibration

The overall hysteresis of the monochromator motor control causes an energy offset, a key experimental systematic which contributes uncertainty to the monochromator-recorded encoder angle. This is obvious for all motor or monochromator systems required to be characterized for its correction. However, calibrated energy is much more reliable over the encoder settings, and much more reliable compared with calibration with an uncalibrated standard foil edge of intermediate thickness (Tantau *et al.*, 2014).

Energy calibration is important for accurate determination of the photoelectron wavenumber *k* (related to measured energy), the Fermi level $E_{\rm F}$ and the XAFS amplitudes. These parameters are directly related to structural information.

Fig. 11 shows the energy correction to the nominal energies recorded by the monochromator. The BigDiff powder diffractometer at the ANBF, Tsukuba, Japan, was used to measure selected energies covering the complete range of

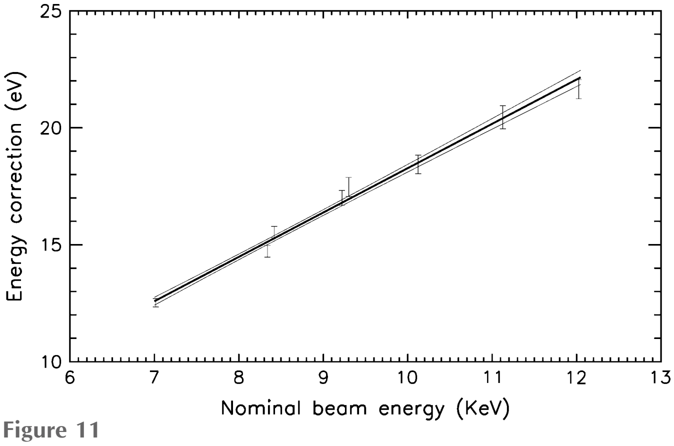

Figure 11
Energy correction to the nominal energy of the X-ray beam. The solid black line represents the fitted line and the thin lines are the 1σ uncertainty. The measured energies are represented by the error bars. The uncertainty was less than 0.5 eV across the entire range and about 0.1 eV across the XAFS region.

energies for the attenuation measurements. A NIST powder standard, Si(640b), was used (the most accurate standard in the literature) for the calibration. Four image plates were used to record diffraction peaks over a broad range of diffracting angles. A least-squares fitting procedure was performed to define the differences between monochromator-recorded nominal energies and calibrated energies.

The use of the BigDiff diffractometer at the ANBF was challenging because it had suffered some damage during the disastrous Tohoku earthquake and Tsunami in Japan. After the disaster, we were the first users of BigDiff for energy calibration, following an investigation of the status of the diffractometer. After the re-establishment of BigDiff by C. T. Chantler, S. P. Best *et al.*, the equipment was used successfully for energy calibration. In fact, the performance was the best it had ever been, with high accuracy (Tantau *et al.*, 2014).

4.4. Harmonic contamination and correction

Measurements using attenuating foils of different thicknesses were carried out using a downstream 'daisy wheel'. A total of eight energies were selected for harmonic measurements covering the complete energy range. A downstream daisy wheel containing a total of 15 aluminium foils around its perimeter was used to measure the attenuations of the mounted daisy foils. The tabulated X-ray mass attenuation coefficients of aluminium (FFAST; Chantler, 2000) were used to characterize and correct for harmonic effects in the X-ray beam.

Higher-order reflections can contribute harmonic components to the incident X-ray beam for selecting a particular energy of the beam by the monochromator (Barnea & Mohyla, 1974). The measured attenuation for a fundamental energy E_1 contaminated by only one harmonic component of energy E_n is given by

$$\exp\left(-\left[\frac{\mu}{\rho}\right][\rho t]\right) = (1-f_n)\exp\left(-\left[\frac{\mu}{\rho}\right]_{E_1}[\rho t]\right) + f_n\exp\left(-\left[\frac{\mu}{\rho}\right]_{E_n}[\rho t]\right), \qquad (14)$$

where f_n is the fraction of the harmonic component of energy E_n present in the fundamental energy. A 0.02–0.1% harmonic contamination was observed at energies from 8.5 keV down to 7.5 keV. Fig. 12 shows the harmonic fraction determined using the fitted function [equation (14)] at 8.21 keV, close to the absorption edge.

4.4.1. Fitting procedure and correction. A total of five parameters (harmonic fraction, f_n; attenuation $[\mu/\rho][\rho t]_{E_1}$ for the fundamental energy E_1; attenuation $[\mu/\rho][\rho t]_{E_3}$ for the third-order energy E_3; a dark-current correction; and an offset) were fitted using the harmonic model [equation (14)] to obtain the harmonic content on the measurements. The best fit (with lowest χ_r^2) was obtained by constraining the $[\mu/\rho][\rho t]_{E_3}$ parameter to the tabulated values at higher energies, and leaving it as a free parameter at lower energies where the harmonic content was large, while the critical output $[\mu/\rho][\rho t]_{E_1}$ for the fundamental energy was unconstrained at all energies.

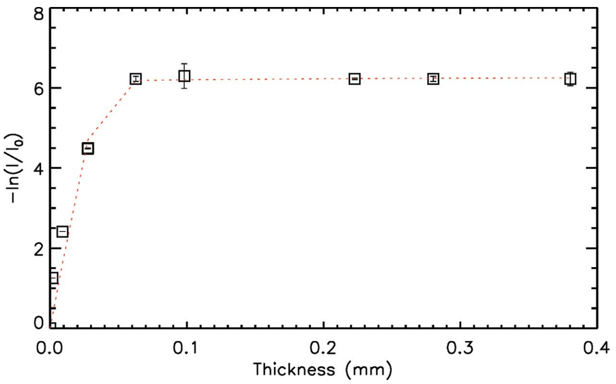

Figure 12
Fitted harmonic content at 8.21 keV for square planar nickel(II) complex. The fitted model returned a fractional contribution of harmonic contamination 0.00088 ± 0.00007 at 8.21 keV close to the edge energy.

The effect of harmonics on the attenuations of the solutions was then corrected for, making use of the fractional contributions at each energy by reversing equation (14). This procedure removes the unwanted attenuation for the higher-order Bragg peaks from the attenuations for the fundamental energies. Harmonic effects up to 0.1% at energies lower than 8.4 keV were observed, while 0.1% was found at energies close to the edge energy 8.332 eV.

5. Result and discussion

The structure and XANES are very well defined for the 15 m*M* solutions with very small uncertainty. This can be used for the development of theory in complex and dilute systems, for the evaluation of the significance of matrix contributions (solvent, water) to the XAFS structure, for the determination of Fermi energies and near-edge structure, for extended XANES analysis and for full analysis of the photoelectron scattering and fine structure; or, of course, for conventional and advanced XAFS analysis.

Particularly important is the result that these uncertainties are well defined and remarkably small (Figs. 13 and 14), so that all studies involving concentrated solutions, or 'dilute systems' above about 3 m*M*, are amenable to *absorption* spectroscopy, in addition to the possibility of fluorescence spectroscopy. One key advantage to date is that the uncertainties can be well defined and propagated to analytical packages, so that hypothesis testing can be made on a rigorous footing. Perhaps just as importantly, these measurements were obtained with a relatively low-flux beamline at ANBF, while the precision and accuracy of the methodology will be much enhanced at more powerful beamlines.

X-ray absorption spectra of the bis(*N*-i-propyl-salicylaldiminato) and bis(*N*-n-propyl-salicylaldiminato) nickel(II) complexes were determined on an absolute scale using the intensity measurements with multiple solutions, and their corresponding solvents. For (i-pr Ni), a 0.1–0.7% accuracy was obtained on a relative scale above the *K*-absorption edge

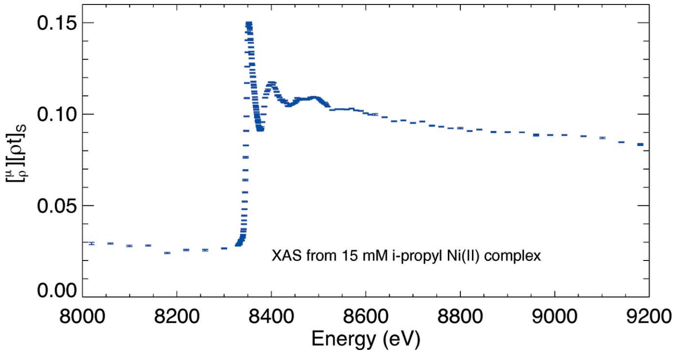

Figure 13
The final XAS of 15 m*M* (i-pr Ni) at the calibrated energies obtained from the weighted mean of multiple measurements (Fig. 8). The weighted uncertainty was determined using the relative uncertainty of the multiple values at each energy.

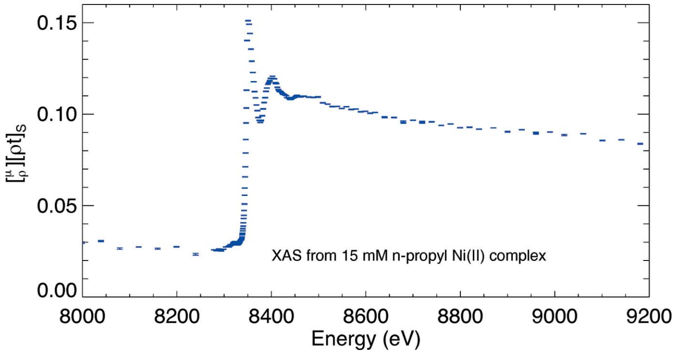

Figure 14
The final corrected XAS of 15 m*M* (n-pr Ni) at the calibrated energies following the correction of key experimental systematics including energy calibration, dark current, harmonic contamination and the scattering effect. The weighted uncertainty was determined using the relative uncertainty of the multiple values at each energy. An apparent discontinuity at 8500 eV is in fact real structure.

(8340.10 eV), where the accuracy varies from 0.4% to 1% on the absolute scale above the edge. For the complete energy range, the accuracy approached 2.6% in the pre-edge region (where the contribution is very small and the background subtraction is most significant). For (n-pr Ni), the accuracy varied from 0.1% to 0.5% above the edge, and approached 2% in the pre-edge region on the relative scale. On the absolute scale, the accuracy varied from 0.2% to 0.6% above the edge, and approached 2.6% in the pre-edge region.

6. Conclusions

We have shown that, with careful attention to the experimental design, XAS can be measured with high and quantified accuracy and precision from m*M* solution samples. The experimental data needed for correction of the systematic errors most commonly impacting on such measurements have been identified and systematized using the so-called hybrid technique. The hybrid technique has been shown to allow measurement of mass attenuation coefficients of solute species in m*M* solutions with an absolute accuracy of 1–5% and relative accuracy of 0.1–0.5%, excluding uncertainties in the offset, over the range used for XAFS analysis. In subsequent publications we will demonstrate that observations of this sort can be used to correct fluorescence measurements and that XAS measurements can impact significantly on the quality of analysis able to be extracted. It is important to note that the systematic errors can lead to offsets, linear and quadratic functionals and/or modulation of the background signal. Conventionally, these effects are obscured by subtraction of an arbitrary spline function. While this practice greatly simplifies the application of XAFS techniques, it also prevents proper error analysis. The availability of accurate observations of the sort presented in this investigation will allow properly validated structural information to be extracted from metal complexes in dilute systems and solutions.

These are the first high-accuracy absorption measurements from isomers using solution samples with m*M* concentrations and proves that this level of accuracy is possible for all solution measurements using absorption. X-ray photoabsorption coefficients and X-ray mass attenuation coefficients for the Raleigh and Compton scattering were determined on a relative scale using the tabulated X-ray mass attenuation data of the complex (FFAST; Chantler, 2000). Comparisons between the measured $[\mu/\rho]$ of the isomers and the theoretical baseline represent the precision of the measurements (Fig. 15).

This study was performed as the first trial on a relatively low-flux beamline. Data quality for analogous experiments at higher-flux beamlines will improve with the photon statistics so that a data quality corresponding to that of the 15 m*M* solutions in this paper will be obtainable for dilutions down to 1.5 m*M* and lower.

In this experiment the 1.5 m*M* solutions were able to give the critical normalization signal and a well defined zero limit together with the background. Although, of course, the individual uncertainties for the 1.5 m*M* data set were much worse than those for the 15 m*M* solutions (see Tables S1, S2 and S3 of the supporting information), improvements of technique

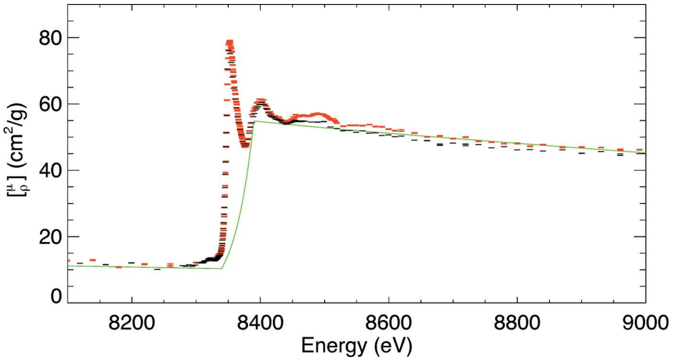

Figure 15
Comparison between the X-ray mass attenuation coefficients of (i-pr Ni) (red) and (n-pr Ni) (black) measured using the intensity measurements with 15 m*M* solutions of each of the complexes (isomers). The impact of the conformation change is dramatic and easily observed. The green solid line shows the tabulated theoretical values (FFAST; Chantler, 2000) with no oscillations. Notice that at high energies there is an offset between the solutions. This is because the relative uncertainty has been plotted but the uncertainty in absolute scaling is dominant and is about 1%. We plot the relative uncertainty because this is the relevant uncertainty for XAFS analysis in the sequel paper.

will result in better control of these error bars. Nonetheless, even the weak 1.5 mM solution has excellent data quality for determination of the Fermi energy, the edge-jump, the XANES and the low-energy EXAFS.

In this investigation we have demonstrated that very high accuracy data sets can be obtained from transmission XAS measurements from dilute solutions that are amenable for further analysis, and indeed for possible *ab initio* analysis of the unknown structures, as will be developed in the sequel paper. Without the statistical development and normalization of the hybrid technique, the signal-to-background would have completely dominated the interpretation of XAFS, and significant information content present in the synchrotron absorption data would have been lost. The data collection and processing presented here permits the exploitation of the full information content of the XAS measurements from dilute samples.

Acknowledgements

The Australian Research Council (ARC) and the Science Faculty of the University of Melbourne are acknowledged for funding this work. The authors would like to thank the staff of the Australian National Beamline Facility (ANBF), Tsukuba, Japan, where the experiment was performed for their assistance in this work. As the ANBF is now closed, we dedicate this work to the efforts of the Australian and Japanese scientists who have worked together to make the beamline and collaboration such a success.

References

Barnea, Z. & Mohyla, J. (1974). *J. Appl. Cryst.* **7**, 298–299.
Bearden, A. J. (1966). *J. Appl. Phys.* **37**, 1681–1692.
Bourke, J., Chantler, C. & Witte, C. (2007). *Phys. Lett. A*, **360**, 702–706.
Britton, D. & Pignolet, L. H. (1989). *Acta Cryst.* C**45**, 819–821.
Chantler, C. T. (2000). *J. Phys. Chem. Ref. Data*, **29**, 597–1048.
Chantler, C. T. (2009). *Eur. Phys. J.* **169**, 147–153.
Chantler, C. T. (2010). *Radiat. Phys. Chem.* **79**, 117–123.
Chantler, C. T., Barnea, Z., Tran, C. Q., Tiller, J. & Paterson, D. (1999). *Opt. Quant. Elect.* **31**, 495–505.
Chantler, C. T., Rae, N. A., Islam, M. T., Best, S. P., Yeo, J., Smale, L. F., Hester, J., Mohammadi, N. & Wang, F. (2012). *J. Synchrotron Rad.* **19**, 145–158.
Cooper, M. J. (1965). *Acta Cryst.* **18**, 813.
Cotelesage, J. J. H., Pushie, M. J., Grochulski, P., Pickering, I. J. & George, G. N. (2012). *J. Inorg. Biochem.* **115**, 127–137.
Cramer, S. P., Tench, O., Yocum, M. & George, G. N. (1988). *Nucl. Instrum. Methods Phys. Res. A*, **266**, 586–591.
Creagh, D. C. & Hubbell, J. H. (1987). *Acta Cryst.* A**43**, 102–112.
Creagh, D. C. & Hubbell, J. H. (1990). *Acta Cryst.* A**46**, 402–408.
Dau, H., Liebisch, P. & Haumann, M. (2003). *Anal. Bioanal. Chem.* **376**, 562–583.
Deslattes, R. D. (1959). PhD thesis, The Johns Hopkins University, Baltimore MD, USA.
Deslattes, R. D. (1969). *Acta Cryst.* A**25**, 89–93.
Diaz-Moreno, S. (2012). *J. Synchrotron Rad.* **19**, 863–868.
Fox, M., Lingafelter, E., Orioli, P. & Sacconi, L. (1963). *Nature (London)*, **197**, 1104.
Fox, M. R., Orioli, P. L., Lingafelter, E. C. & Sacconi, L. (1964). *Acta Cryst.* **17**, 1159–1166.
Furenlid, L., Kraner, H., Rogers, L., Cramer, S., Stephani, D., Beuttenmuller, R. & Beren, J. (1992). *Nucl. Instrum. Methods Phys. Res. A*, **319**, 408–413.
Gerward, L., Thuesen, G., Stibius Jensen, M. & Alstrup, I. (1979). *Acta Cryst.* A**35**, 852–857.
Glover, J. L., Chantler, C. T., Barnea, Z., Rae, N. A. & Tran, C. Q. (2010). *J. Phys. B*, **43**, 085001.
Glover, J. L., Chantler, C. T. & de Jonge, M. D. (2009). *Phys. Lett. A*, **373**, 1177–1180.
Goulon, J., Goulon-Ginet, C., Cortes, R. & Dubois, J. (1982). *J. Phys. Fr.* **43**, 539–548.
Grodstein, G. W. (1957). *X-ray attenuation coefficients from 10 keV to 100 MeV.* Technical Report. DTIC Document.
Hubbell, J. H. (1969). *Photon cross sections, attenuation coefficients, and energy absorption coefficients from 10 keV to 100 GeV.* Technical Report. DTIC Document.
Hughes, G., Woodhouse, J. & Bucklow, I. (1968). *J. Phys. D*, **1**, 695–706.
Islam, M. T., Rae, N. A., Glover, J. L., Barnea, Z. & Chantler, C. T. (2010). *Nucl. Instrum. Methods Phys. Res. A*, **619**, 44–46.
Islam, M. T., Tantau, L. J., Rae, N. A., Barnea, Z., Tran, C. Q. & Chantler, C. T. (2014). *J. Synchrotron Rad.* **21**, 413–423.
Jaklevic, J., Kirby, J., Klein, M., Robertson, A., Brown, G. & Eisenberger, P. (1977). *Solid State Commun.* **23**, 679–682.
Joly, Y. (2001). *J. Phys. B*, **63**, 125120.
Joly, Y., Cabaret, D., Renevier, H. & Natoli, C. R. (1999). *Phys. Rev. Lett.* **82**, 2398–2401.
Jonge, M. D. de, Tran, C. Q., Chantler, C. T., Barnea, Z., Dhal, B. B., Cookson, D. J., Lee, W. K. & Mashayekhi, A. (2005). *Phys. Rev. A*, **71**, 032702.
Kessler, E. Jr, Deslattes, R., Girard, D., Schwitz, W., Jacobs, L. & Renner, O. (1982). *Phys. Rev. A*, **26**, 2696–2706.
Kodre, A., Padežnik Gomilšek, J., Mihelič, A. & Arčon, I. (2006). *Radiat. Phys. Chem.* **75**, 188–194.
Kopfmann, G. & Huber, R. (1968). *Acta Cryst.* A**24**, 348–351.
Kurisaki, T., Matsuo, S., Tóth, I. & Wakita, H. (2008). *Anal. Sci.* **24**, 1385–1392.
McMaster, W., Del Grande, N. K., Mallett, J. & Hubbell, J. (1969). In *Rep. TID-4500, UC-34, Physics.* Lawrence Radiation Laboratory, University of California Livermore, USA.
Meitzner, G. & Fischer, D. (2002). *Microchem. J.* **71**, 281–286.
Meulenaer, J. de & Tompa, H. (1965). *Acta Cryst.* **19**, 1014–1018.
Mika, J. F., Martin, L. J. & Barnea, Z. (1985). *J. Phys. C*, **18**, 5215–5223.
Nathuram, R., Sundara Rao, I. S. & Mehta, M. K. (1988). *Phys. Rev. A*, **37**, 4978–4981.
Penner Hahn, J. E. (1999*a*). *CCC01063, X-ray Absorption Spectroscopy.* The University of Michigan, Ann Arbor, MI, USA.
Penner-Hahn, J. E. (1999*b*). *Coord. Chem. Rev.* **190–192**, 1101–1123.
Pettifer, R. F., Mathon, O., Pascarelli, S., Cooke, M. D. & Gibbs, M. R. (2005). *Nature (London)*, **435**, 78–81.
Pfalzer, P., Urbach, J.-P., Klemm, M., Horn, S., denBoer, M. L., Frenkel, A. I. & Kirkland, J. P. (1999). *Phys. Rev. B*, **60**, 9335–9339.
Prešeren, R., Kodre, A., Arčon, I. & Borowski, M. (2001). *J. Synchrotron Rad.* **8**, 279–281.
Rae, N. A., Chantler, C. T., Barnea, Z., de Jonge, M. D., Tran, C. Q. & Hester, J. R. (2010). *Phys. Rev. A*, **81**, 022904.
Rao, V. V., Shahnawaz & Rao, D. V. (1981). *Physica B+C*, **111**, 107–110.
Tantau, L., Islam, M., Payne, A., Tran, C., Cheah, M., Best, S. & Chantler, C. (2014). *Radiat. Phys. Chem.* **95**, 73–77.
Tran, C. Q., Barnea, Z., de Jonge, M. D., Dhal, B. B., Paterson, D., Cookson, D. J. & Chantler, C. T. (2003). *X-ray Spectrom.* **32**, 69–74.
Zhang, K., Rosenbaum, G. & Bunker, G. (1998). *J. Synchrotron Rad.* **5**, 1227–1234.